



Sensitive Biosensors Based on Plasmonic-graphene Nanocombinations for Detection of Biological Elements in Blood Samples

Roozbeh Negahdari^{1,2} · Esmat Rafiee³ · Farzin Emami^{1,2,4}

Received: 27 January 2023 / Accepted: 6 March 2023 / Published online: 20 March 2023
© The Author(s), under exclusive licence to Springer Science+Business Media, LLC, part of Springer Nature 2023

Abstract

In this work, a sensitive biosensor is proposed and investigated based on the combinations of graphene-plasmonic nanostructures. The suggested structure is made of different layers of SiO₂, gold (Au), and graphene in the formats of U-shaped, split ring, and straight waveguides. Straight waveguides which are connected to the U-shaped waveguides are denoted as the Input, Output1, Output2, and Output3 ports. The incident light-wave would be applied to the Input port and then would be transmitted to the three output ports with different peak wavelengths (considering the specifications of the structure). In the proposed structure, for improving its functionalities (improving the transmission's peak value and wavelength for bio-sensing applications), effects of different structural parameters ($w_1, t_1, g_1, w_2, t_2, g_2, w_3, t_3, \text{ and } g_3$) and chemical potentials ($\mu_{c1}, \mu_{c2}, \text{ and } \mu_{c3}$) are considered. After improving the structure's transmission spectrum at different output ports (Output1, Output2, and Output3 ports), vital biological element's concentrations in blood samples (glucose, cholesterol, and creatinine concentrations) would be considered for diagnosis. Finally, considerable sensitivity factors of 1560 nm/RIU "RIU stands for refractive index unit" (for glucose at Output1 port), 2666.6 nm/RIU (for cholesterol at Output2 port), and 1458.3 nm/RIU (for creatinine at Output3 port) are obtained. Also, FWHM and FOM of "13 nm, 120," "19 nm, 76.75," and "15 nm, 177.77" are achieved for glucose, creatinine, and cholesterol, respectively. Therefore, the structure can be considered as an appropriate and efficient candidate for biosensing applications in optical integrated circuits.

Keywords Bio-sensor · Cholesterol · Creatinine · Glucose · Plasmonic-graphene · Optical integrated circuits

Introduction

Biosensor is basically a device which measures biological or chemical reactions. This measurement can be done by generating signals which are proportional to the concentration

of the analyte in the reaction. Optical biosensors are among the most efficient and functional biosensors due to their highest speed of detection, sensitives, integration abilities (can be fabricated in very small dimensions by utilizing plasmonic-graphene combinations), lower costs, and highest efficiencies [1, 2]. Optical biosensors are very compact devices emitting signals proportional to the concentration of the analyte which is in contact with the biological elements (biological elements like enzymes, antibodies, antigens, etc.) These devices (optical biosensors) can be considered based on various optical configurations like plasmonic [3], graphene [4], plasmonic-graphene [2, 5], and ... combinations. Plasmonic-graphene nanostructures mainly indicate high optical confinement, flexibility in designation, and considerable efficiencies [6]. Therefore, they can be appropriate candidates for constructing sensitive biosensors. These optical nanostructures mainly operate based on surface plasmon resonance (SPR) effect [7, 8], which makes them appropriate choices in extremely low-dimensional structures (lower than the operating wavelength). As known, plasmonic structures

✉ Esmat Rafiee
e.rafee@alzahra.ac.ir
Roozbeh Negahdari
r.negahdari@sutech.ac.ir
Farzin Emami
emami@sutech.ac.ir; farzin.emami@deakin.edu.au

¹ Shiraz, Iran
² Electronic Department, Nano-Optoelectronic Research Center, Shiraz University of Technology, Shiraz, Iran
³ Department of Electrical Engineering, Faculty of Engineering, Alzahra University, Tehran, Iran
⁴ Center for Smart Power and Energy Research, School of Engineering, Deakin University, Melbourne, Australia

are based on the combination of metal-dielectric layers. On the other hand, graphene nanostructures are mainly based on the layers of carbon atoms which are ordered in two-dimensional lattices [5, 6]. SPR effect can help in surpassing the diffraction limits of light in plasmonic-graphene nanostructures [2]. Plasmonic-graphene nanostructures can be considered based on various configurations, in which split ring resonator-shaped waveguides are of great interest (due to their higher tunability, efficiencies, and integrations) [9, 10]. Graphene-plasmonic nanostructures can be fabricated based on different techniques like electron-beam lithography, focused-ion lithography, dip-pen lithography, laser interference lithography, and nanosphere lithography [11–15].

As stated biosensors can be considered for detection of various biological elements like hemoglobin [2], glucose [16], creatinine [17], cholesterol [18], and triglyceride [19]. As known, glucose is a type of sugar which can be measured by a blood test. It is a very important element in the blood which can indicate serious diseases (high or low concentration of glucose in blood samples). Another important element in blood is creatinine which is responsible for indicating health condition of kidneys. Cholesterol is also another important element in blood showing possible risks of heart diseases [16–18].

Many researchers have focused and worked on the plasmonic-graphene sensors for detection of various elements. In [20], a sensitive biosensor based on silver nanorods in square resonator was proposed and considered. The proposed biosensor was applied for detection of various human blood groups (A, B, and O) with the sensitivity factor of 2320 nm/RIU. In another research [21], a sensitive refractive index sensor (measuring the refractive index differences and temperature) considering metal-insulator-metal (MIM) configuration was proposed. The structure attained the refractive index and temperature sensitivity factors of 2610 nm/RIU and 1.03 nm/C, respectively. In [22], a biosensor based on MIM racetrack resonator structure was considered with the refractive index and temperature sensitivity factors of 4650 nm/RIU and 0.69 nm/C. Also, in [23], a refractive index biosensor based on two MIM waveguides and arrays of hexagonal nanoholes was proposed for detection of human blood group with the sensitivity factor of 3172 nm/RIU. In [24], by considering plasmonic-induced transparency (PIT) effect, a sensitive sensor for detection of ultra-low concentrations of analyte (ethanol and water) was proposed. For the proposed structure, refractive index, temperature, and pressure sensitivities of 1271 nm/RIU, 0.47 nm/C, and 5 nm/MPa for ethanol were obtained. Also, in [25], by utilizing an elliptical resonator and MIM waveguide, a sensitive sensor was achieved with the sensitivity and FOM of 550 nm/RIU and 282.5 RIU⁻¹, respectively. In another research [26], by considering various H-shaped cavities, three different

refractive index sensors were proposed with the FOM values of 69.5, 100.19, and 108.36 RIU⁻¹, respectively.

In [3], a refractive index (RI) biosensor based on Si nanorings and plasmonic ring-shaped arrays were proposed for detection of glucose concentrations in water solution. The structure indicated acceptable sensitivity and figure of merit (FOM) of 1278 nm/RIU and 168.1 RIU⁻¹, respectively. In another research [27], by utilizing a graphene mono-layer and applying gate voltage, an SPR glucose sensor was proposed. In [28], by developing a gold electrode with a graphene quantum dot and utilizing square-wave method, creatinine levels in blood and urine were detected. Also, in [29], for monitoring cholesterol in human serum, a biosensor based on graphene quantum dots and zirconium-based metal-organic framework nanocomposite was suggested. Moreover, in [30], cholesterol concentrations were measured by using graphene oxide sheet-based sensors. In this research, new and precise biosensors based on graphene-plasmonic nanocombinations for detection of different biological elements (glucose, creatinine, and cholesterol) are proposed. Configuring sensitive biosensors based on the plasmonic-graphene combinations are the most important aspects of the proposed manuscript. The proposed structure's ability (novelty) is mainly the possibility of diagnosing the concentrations of three individual biological elements (glucose, creatinine, and cholesterol) with remarkable sensitivity factors.

Geometry and Theoretical Model

Schematic of the proposed plasmonic-graphene nanostructure is presented in Fig. 1.

As seen in Fig. 1, the structure is consisted of an inner split ring-shaped waveguide (with one split) and an outer split ring-shaped waveguide (with four splits). The four individual parts of the outer split ring are connected to four straight waveguides and are denoted as Input, Output1, Output2, and Output3 ports. As shown in Fig. 1, the whole structure is based on layers of Au (Gold), SiO₂, and graphene. The geometric parameters of Fig. 1 are tabulated in Table 1.

Numerical simulations were conducted by using two-dimensional finite element-based (FE) software (COMSOL Multiphysics 5.5).

In the proposed structure, the transmission spectrum would be considered. Thus, the relation between the transmission, absorption, and reflection fields would be considered in Eq. (1) [2, 31].

$$A(\omega) = 1 - R(\omega) - T(\omega) \quad (1)$$

It is clear that $T(\omega) = 1 - R(\omega)$ if $A(\omega) = 0$.

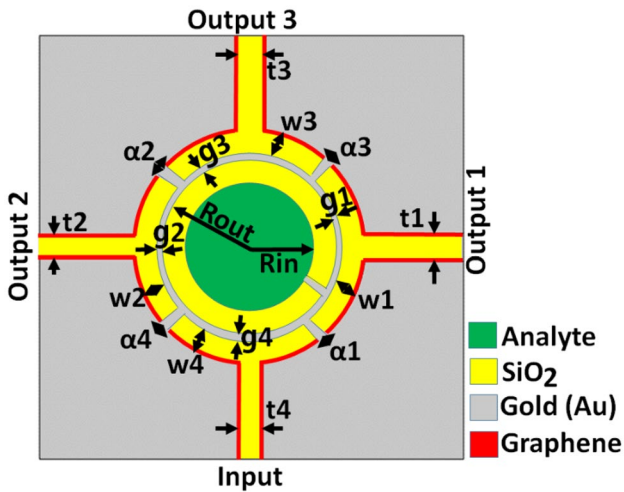


Fig. 1 View of the proposed plasmonic-graphene nanostructure

As known, higher transmission values lead to higher output fields at different ports (Output1, Output2, and Output3 ports).

As shown in Fig. 1, different graphene layers are considered around the SiO₂ curved T-shaped layers. The surface conductivity of the graphene layers can be calculated by the Kubo formula [2, 31, 32]:

$$\sigma_g(\omega, \mu_c, \Gamma, T) = \sigma_{g-real} + j\sigma_{g-imag} = \sigma_{intra} + \sigma_{inter} \quad (2)$$

where ω , μ_c , Γ , and T represent the operation frequency, chemical potential, phenomenological scattering rate, and absolute temperature, respectively.

Table 1 Geometric parameters of Fig. 1

Parameter	Value (nm)
t_1	20
w_1	20
g_1	4
α_1	2°
t_2	20
w_2	20
g_2	3
α_2	3°
t_3	20
w_3	20
g_3	4
α_3	4
t_4	20
w_4	20
g_4	3
α_4	2°
R_{in}	295
R_{out}	325

The intra- and inter-band electro-photon scattering parameters can also be considered as [2, 31, 32]:

$$\sigma_{intra} = -j \frac{e^2 k_B T}{\pi \hbar^2 (\omega - j2\Gamma)} \times \left[\frac{\mu_c}{k_B T} + 2 \ln \left(\exp \left(-\frac{\mu_c}{k_B T} \right) + 1 \right) \right] \quad (3)$$

$$\sigma_{inter} = -j \frac{e^2}{4\pi \hbar} \ln \left[\frac{2|\mu_c| - (\omega - j2\Gamma)\hbar}{2|\mu_c| + (\omega - j2\Gamma)\hbar} \right] \quad (4)$$

where k_B , T , and e are Boltzmann constant, temperature, and electron charge, respectively.

For the Au waveguides considered in the proposed structure, Drude model can be used for introducing the dielectric function [9, 10]:

$$\epsilon(\omega) = \epsilon_\infty - \frac{\omega_p^2}{\omega^2 - j\omega\gamma} \quad (5)$$

where $\epsilon_\infty = 3.7$ (dielectric constant at infinite frequency), $\gamma = 0.018$ eV (collision plasma angular frequency), and $\omega_p = 9.1$ eV (bulk plasma angular frequency) [9, 10].

Various filtering wavelength ranges at the three output ports (Output1, Output2, and Output3) can be obtained, if different split angles (for the outer split ring) would be considered. In the following parts, for improving the functionality of the structure at the three output ports (improving the transmission's peak value and wavelength), effects of different structural parameters and chemical potentials would also be considered. Finally, three output ports would be considered as sensors for detecting various biological elements in blood samples like glucose, creatinine, and cholesterol.

Results and Descriptions

In this part, the incident field (a plane wave polarized in z-axis with 1 W power) would be applied to Input port and the transmitted signals would be considered at Output1, Output2, and Output3 ports. As stated, for improving the transmission's peak value and wavelength (to be utilized as sensitive biosensors), effects of different structural parameters (w_1 , t_1 , g_1 , w_2 , t_2 , g_2 , w_3 , t_3 , and g_3) and chemical potentials (μ_{c1} , μ_{c2} , and μ_{c3}) would be considered.

Transmitted Signal at Output1

In this part, signal transmitted to Output1 would be considered. Effects of structural parameters (w_1 , t_1 , and g_1) and chemical potential of the graphene layer (μ_{c1}) would also be investigated. The results are presented in the following sections.

Effects of “ w_1 ”

In the first section, for improving the functionality of the structure (mainly improving the transmission’s peak value), effects of “ w_1 ” on the transmission spectrum are investigated and shown in Fig. 2.

As shown in Fig. 1, w_1 is the width of the right-handed u-shaped waveguide (related to Output1). It can be concluded from Fig. 2 that increasing “ w_1 ” from 9 to 17 nm moves the transmission’s peak wavelength and value to higher amounts.

It should be noted that, by using the temporal coupled-mode theory [33–36], the transmission “ T ” of system can be described as:

$$T = \frac{(\omega - \omega_0)^2 + \left(\frac{1}{\tau_0}\right)^2}{(\omega - \omega_0)^2 + \left(\frac{1}{\tau_0} + \frac{1}{\tau_e}\right)^2} \tag{6}$$

where $\omega = 2\pi c/\lambda$, ω_0 , $1/\tau_0$, and $1/\tau_e$ stand for the frequency, the resonant frequency, the decay rate of the field (due to the internal loss), and the decay rate (due to the power outflow of the waveguide). The resonant wavelength λ_0 (transmission’s peak wavelength) can be controlled by the geometry parameters like the length “ t_1, t_2, t_3 , and t_4 ” and the width “ w_1, w_2, w_3 , and w_4 .” In the following equation, “ t ” can be replaced by “ w .”

$$\Delta\phi = \frac{4\pi \cdot \text{Re}(n_{\text{eff}}) \cdot t}{\lambda_0} \tag{7}$$

where $\Delta\phi = m \cdot 2\pi$ and n_{eff} is the effective refractive index of the waveguide. As can be seen, λ_0 is directly proportional to “ t ” or “ w .” Therefore, by increasing “ t ” or “ w ,” λ_0 would also be increased (red-shifted).

As can be seen, increasing “ w_1 ” decreases the attenuation coefficients which enhances the transmission’s peak value (also increases the coupling coefficient). On the other hand, changing “ w_1 ” from 17 to 23 nm shifts the transmission’s peak wavelength and value to higher and lower amounts,

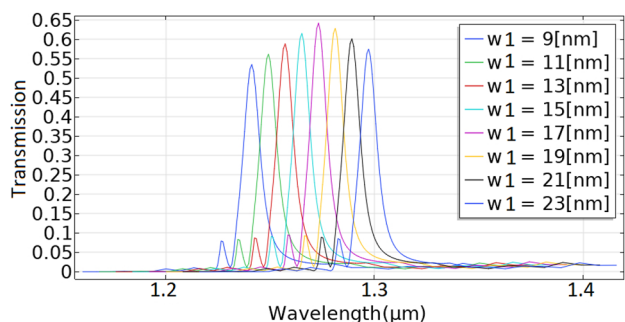


Fig. 2 Schematic of the transmission spectrum versus wavelength for different values of “ w_1 ”

respectively. In this case (considering higher values for w_1), optical confinement of the light wave in the waveguide is extensively increased, which decreases the transmission’s peak values [9, 37]. It can be concluded that increasing the waveguide’s width (up to $w_1 = 17$ nm) can somehow increase the transmission’s peak value (due to the decrement of the attenuation coefficients). In another case (for $w_1 > 17$ nm), the transmission’s peak value would be decreased (due to the enhancement of the optical confinement which leads to lower coupling coefficient). As a result, the improved transmission’s peak value and wavelength of 0.64 and 1.27 μm are obtained for $w_1 = 17$ nm.

Effects of “ t_1 ”

In this section, for improving the functionality of the system at Output1, effects of “ t_1 ” (width of the right-handed waveguide) on the transmission spectrum are investigated and shown in Fig. 3.

As can be seen in Fig. 3, the variation process of “ t_1 ” versus transmission’s peak value is similar to “ w_1 .” In fact, by changing “ t_1 ” from 2 to 3.5 nm, the transmission’s peak value would be shifted to higher value. In another case, changing “ t_1 ” from 3.5 to 20 nm shifts the transmission’s peak value to lower amounts. This can be explained by the fact that increasing the width would firstly decrease the attenuation coefficient (leading to higher transmission’s peak values, also increasing the coupling coefficient) and then would increase the optical confinement (leading to lower transmission’s peak values) [9, 37]. Considering Fig. 3, the improved transmission’s peak value and wavelength of 0.8 and 1.22 μm are achieved for $t_1 = 3.5$ nm. It should be mentioned that the improved parameters obtained in each part would be utilized in the following structures.

Effects of “ g_1 ”

In this part, effects of “ g_1 ” (coupling length between the inner split ring and right-handed u-shaped waveguide “also known as gap”) are studied and depicted in Fig. 4.

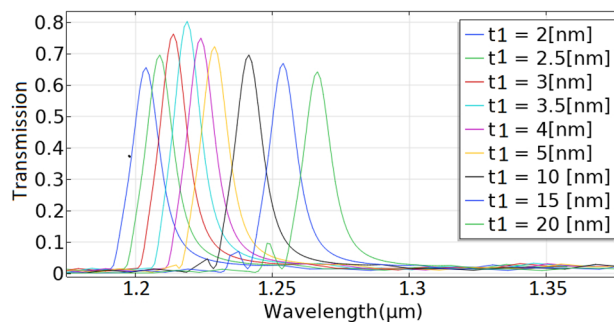


Fig. 3 Schematic of the transmission spectrum versus wavelength for different values of “ t_1 ”

As stated, “ g_1 ” represents the coupling length or gap related to Output1 port. Increasing “ g_1 ” would increase the coupling length which would decrease the coupling coefficient. As a result, the transmission’s peaks value experience lower values (by increasing “ g_1 ”) [36]. It can also be concluded from Fig. 4 that increasing “ g_1 ” would shift the transmission’s peak wavelength to lower values (blue-shift). This can be understood from the resonance condition (from the theory of ring resonator) presented in [38]. Finally, the best result is obtained for $g_1=0.2$ nm with the transmission’s peak value and wavelength of 0.97 and 1.27 μm , respectively. In the following part, effects of “ μ_{c1} ” are considered.

Effects of “ μ_{c1} ”

In this part, effects of “ μ_{c1} ” (chemical potential of the right-sided waveguide) on the transmission spectrum are investigated and depicted in Fig. 5.

As can be seen in Fig. 5, changing “ μ_{c1} ” from 0.3 to 1.1 eV would shift the transmission’s peak value from 0.97 to 0.995. It can also be seen that the transmission’s peak wavelength would experience the blue-shift (moves from 1.27 to 1.24 μm). Variations of the transmission’s peak wavelength can be explained by the circuit theory. As stated in the circuit theory, graphene can be considered as a shunt admittance which is sensitive to the geometrical parameters and chemical potential [2, 31, 39]. As a result, altering “ μ_{c1} ” can affect the transmission’s peak wavelength according to [2, 31, 39]:

$$\lambda = 2\pi c\sqrt{LC} \tag{8}$$

where c , L , and C represent the speed of the light in vacuum, capacitance, and inductance of the circuit respectively. According to Eq. (6), increasing “ μ_{c1} ” decreases \sqrt{LC} , which would also decrease λ (transmission’s peak wavelength).

Thus, the improved transmission’s peak value and wavelength of 0.995 and 1.24 μm are achieved, respectively, for $\mu_{c1} = 1.1$ eV.

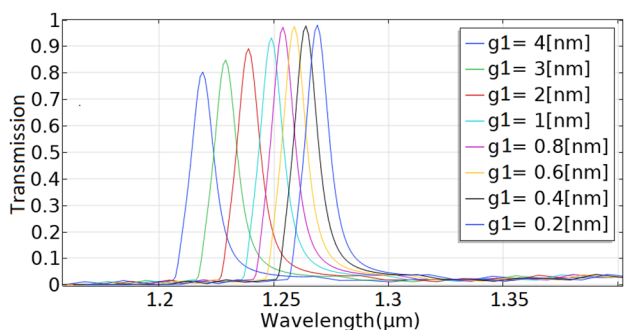


Fig. 4 Schematic of the transmission spectrum versus wavelength for different values of “ g_1 ”

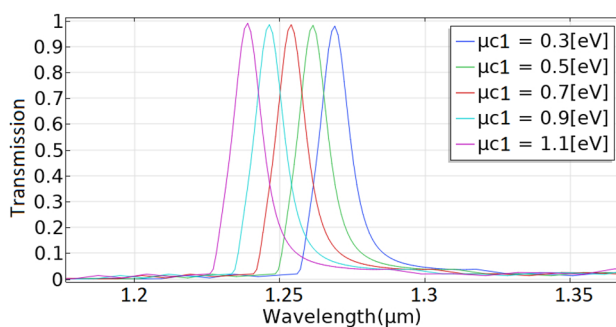


Fig. 5 Schematic of the transmission spectrum versus wavelength for different values of “ μ_{c1} ”

In the last section, field distribution is obtained for Output1 port by considering $\lambda = 1.24$ μm , $w_1 = 17$ nm, $t_1 = 3.5$ nm, $g_1 = 0.2$ nm, and $\mu_{c1} = 1.1$ eV. The field distribution diagram is depicted in Fig. 6.

In the following part, Output2 would be considered, and effects of w_2 , t_2 , g_2 , and μ_{c2} on the transmission spectrum would be investigated.

Transmitted Signal at Output2

In this part, signal transmitted (filtered) to Output2 (left-sided output port) would be considered. Effects of different structural parameters (w_2 , t_2 , and g_2) and chemical potential of the graphene layer (μ_{c2}) on the transmission spectrum would also be studied. The first parameter to be studied is “ w_2 .”

Effects of “ w_2 ”

In this part, effects of “ w_2 ” (width of the u-shaped waveguide of Output2) on the transmission spectrum are investigated and depicted in Fig. 7.

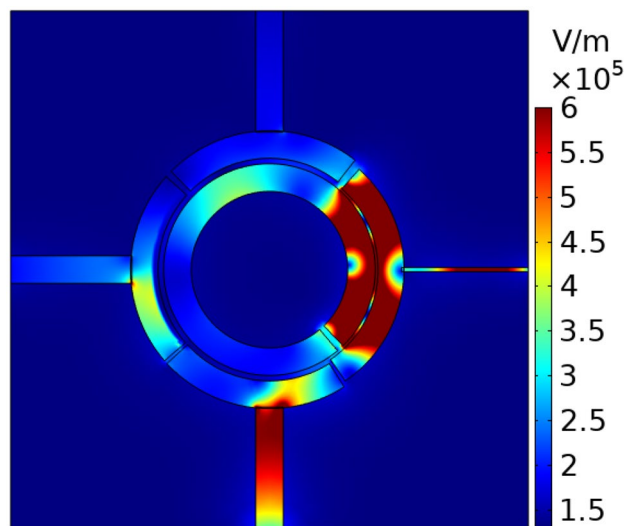


Fig. 6 Field distribution at $\lambda = 1.24$ μm for Output1 port

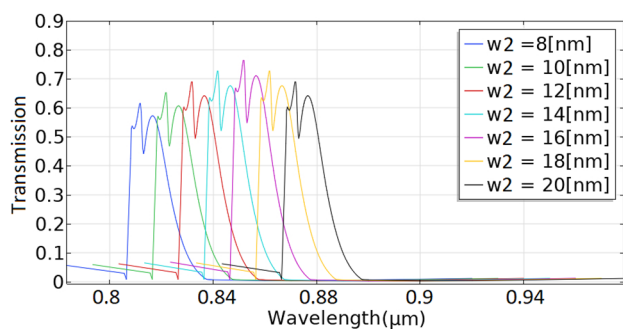


Fig. 7 Schematic of the transmission spectrum versus wavelength for different values of “ w_2 ”

As can be seen in Fig. 7, increasing “ w_2 ” would firstly increase the transmission’s peak value and then decrease it. As stated in the previous sections, increment of the peak value (by increasing the width to some extent) occurs due to the decrement of the attenuation coefficient. On the other hand, for higher values of “ w_2 ,” transmission’s peak value experiences lower values due to the excessively enhanced optical confinement of the light wave (leading to lower coupling coefficient) [9, 37]. It is obviously seen in Fig. 7 that by increasing “ w_2 ” from 8 to 16 nm, the transmission’s peak value moves from 0.6 to 0.78. In another case, by increasing “ w_2 ” from 16 to 20 nm, the transmission’s peak value varies from 0.78 to 0.7. Finally, the improved transmission’s peak value and wavelength of 0.78 and 0.855 μm are obtained for $w_2 = 16$ nm.

Effects of “ t_2 ”

In this part, for enhancing the functionality of the system at Output2, effects of “ t_2 ” (width of the left-handed waveguide) on the transmission spectrum are investigated and shown in Fig. 8.

As can be seen in Fig. 8, t_2 ’s variations versus transmission’s peak values are the same as t_1 ’s (presented in the “Effects of “ t_1 ”” section) [9, 37]. In fact, by changing “ t_2 ”

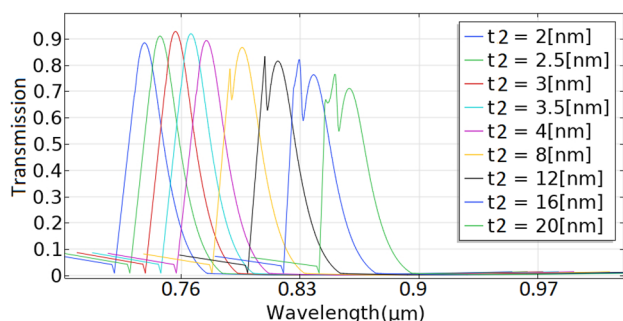


Fig. 8 Schematic of the transmission spectrum versus wavelength for different values of “ t_2 ”

from 2 to 3 nm, the transmission’s peak value would be shifted from 0.89 to 0.92. This phenomenon is the result of the attenuation coefficient decrement (leading to higher coupling coefficient). On the other hand, by changing “ t_2 ” from 3 to 20 nm, the transmission’s peak value would be varied from 0.92 to 0.76, which is due to the enhancement of the optical confinement of light wave in the waveguide (leading to lower coupling coefficient). Therefore, the improved transmission’s peak value and wavelength of 0.92 and 0.759 μm are achieved for $t_2 = 3$ nm.

Effects of “ g_2 ”

In this section, effects of “ g_2 ” (coupling length between the inner split ring and left-handed u-shaped waveguide “also known as gap”) are investigated and shown in Fig. 9.

“ g_2 ” affects the transmission’s peak value and wavelength almost the same as “ g_1 .” As can be seen in Fig. 9, increasing “ g_2 ” decreases the transmission’s peak value and wavelength simultaneously [36, 38]. Decrement of the transmission’s peak value by increasing “ g_2 ” is the result of experiencing lower coupling coefficient [36]. Finally, the best result is obtained for $g_2 = 0.2$ nm with the transmission’s peak value and wavelength of 0.98 and 0.855 μm , respectively.

Effects of “ μ_{c2} ”

In this part, effects of “ μ_{c2} ” (chemical potential of the left-sided waveguide) on the transmission spectrum are investigated and depicted in Fig. 10.

As can be seen in Fig. 10, “ μ_{c2} ” affects the transmission’s peak value and wavelength the same as “ μ_{c1} .” By changing “ μ_{c2} ” from 0.3 to 1.1 eV, the transmission’s peak value and wavelength move from 0.98 to 0.995 and from 0.855 to 0.81 μm , respectively. As previously stated, these variations can be explained by the circuit theory [2, 31, 39].

As a result, the improved transmission’s peak value and wavelength of 0.995 and 0.81 μm are obtained, respectively, for $\mu_{c2} = 1.1$ eV.

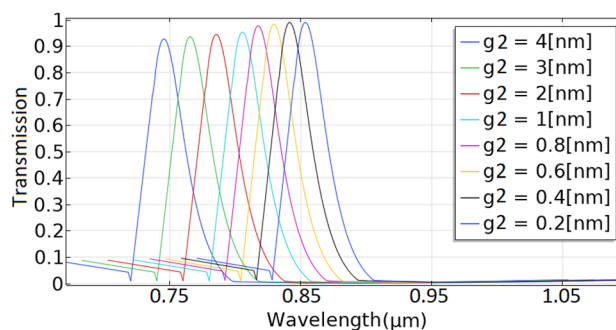


Fig. 9 Schematic of the transmission spectrum versus wavelength for different values of “ g_2 ”

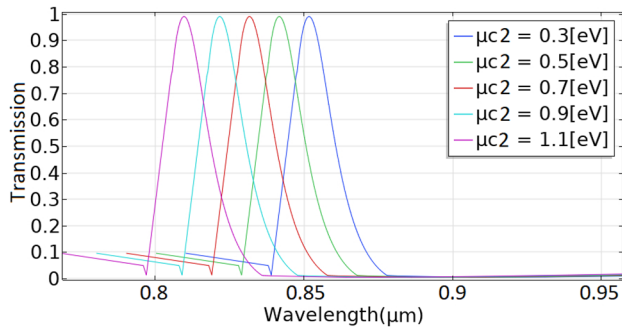


Fig. 10 Schematic of the transmission spectrum versus wavelength for different values of “μ_{c2}”

In the last part, field distribution diagram is considered for Output2 port by considering λ=0.81 μm, w₂=16 nm, t₂=3 nm, g₂=0.2 nm, and μ_{c2}=1.1 eV and is shown in Fig. 11.

In the third section, Output3 would be considered, and effects of w₃, t₃, g₃, and μ_{c3} on the transmission spectrum would be investigated.

Transmitted Signal at Output3

In this part, the signal transmitted to Output3 (upper-side output port) would be considered. Effects of different structural parameters (w₃, t₃, and g₃) and chemical potential of the graphene layer (μ_{c3}) on the transmission spectrum would also be investigated. The first parameter to be considered is “w₃.”

Effects of “w₃”

In this section, effects of “w₃” on the transmission spectrum are considered and shown in Fig. 12.

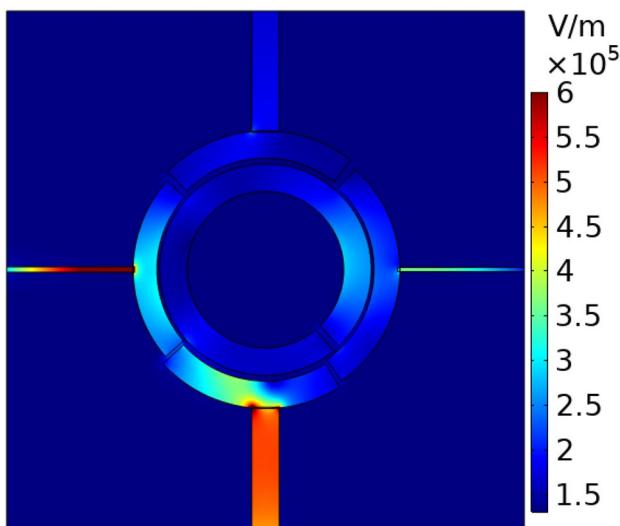


Fig. 11 Field distribution at λ=0.81 μm for Output2 port

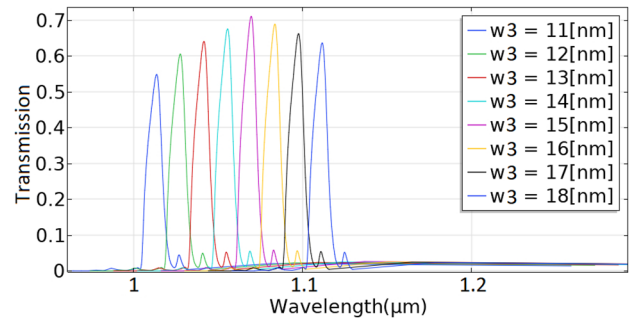


Fig. 12 Schematic of the transmission spectrum versus wavelength for different values of “w₃”

As can be seen in Fig. 12, by increasing “w₃” from 11 to 15 nm, the transmission’s peak value would be enhanced from 0.55 to 0.71. On the other hand, by increasing “w₃” from 15 to 18 nm, the transmission’s peak value would be changed from 0.71 to 0.64. The transmission’s peak wavelength is also red-shifted by increasing “w₃.” Obviously “w₃” affects the transmission’s peak value and wavelength just like “w₁” and “w₂” [9, 37]. Thus, the improved transmission’s peak value and wavelength of 0.71 and 1.07 μm are obtained for w₃=15 nm. In the following part, effects of “t₃” would be considered.

Effects of “t₃”

In this part, for improving the functionality of the system at Output3, effects of “t₃” (width of the upper-sided waveguide) on the transmission spectrum are investigated and depicted in Fig. 13.

It can be seen in Fig. 13 that by enhancing “t₃” from 2.5 to 4 nm, the transmission’s peak value would be shifted from 0.7 to 0.81. In another case, by increasing “t₃” from 4 to 20 nm, the transmission’s peak value would be changed from 0.81 to 0.71. The transmission’s peak wavelength is effectively red-shift by increasing “t₃.” It should be mentioned that “t₃” variation process is the same as “t₁” and “t₂”

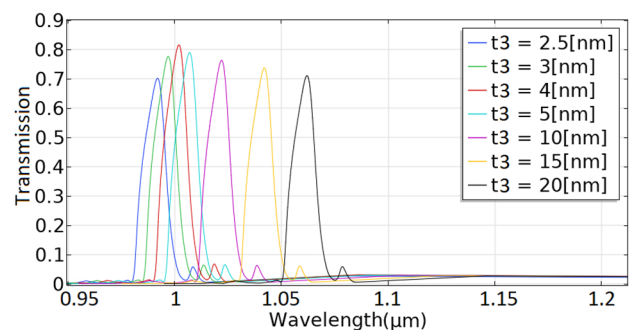


Fig. 13 Schematic of the transmission spectrum versus wavelength for different values of “t₃”

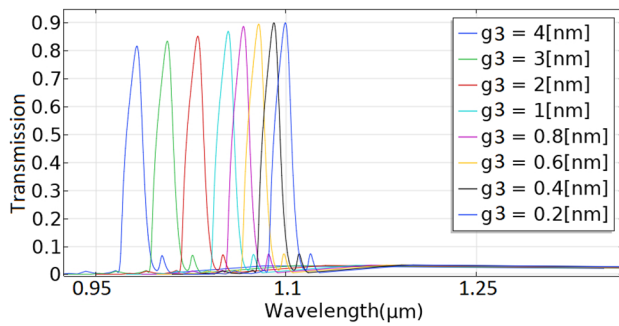


Fig. 14 Schematic of the transmission spectrum versus wavelength for different values of “ g_3 ”

[9, 37]. As a result, the improved transmission’s peak value and wavelength of 0.81 and 1 μm are achieved for $t_3 = 4$ nm.

Effects of “ g_3 ”

In this section, effects of “ g_3 ” (coupling length between the inner split ring and upper-handed u-shaped waveguide) are considered and depicted in Fig. 14.

As indicated in Fig. 14, “ g_3 ” variation process is similar to “ g_1 ” and “ g_2 ” [36, 38]. Therefore, the best result is obtained for $g_3 = 0.2$ nm with the transmission’s peak value and wavelength of 0.9 and 1.1 μm , respectively. In the last part, effects of “ μ_{c3} ” would be considered and investigated.

Effects of “ μ_{c3} ”

In this section, effects of “ μ_{c3} ” (chemical potential of the upper-sided waveguide) on the transmission spectrum are investigated and depicted in Fig. 15.

As can be seen in Fig. 15, by increasing “ μ_{c3} ” from 0.3 to 1.1 eV, the transmission’s peak value and wavelength would be changed from 0.96 to 0.995 and from 1.27 to 1.24 μm , respectively. Obviously “ μ_{c3} ” affects the transmission’s peak value and wavelength just like “ μ_{c1} ” and “ μ_{c2} ” [2, 31, 39].

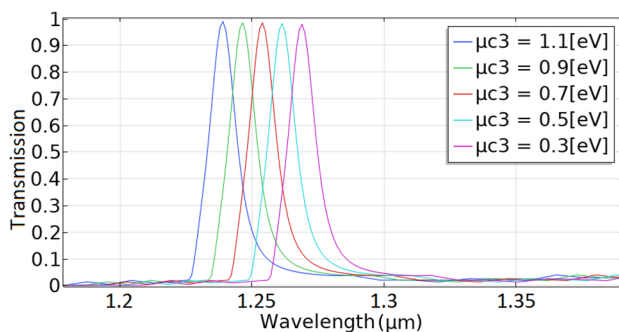


Fig. 15 Schematic of the transmission spectrum versus wavelength for different values of “ μ_{c3} ”

Finally, the improved transmission’s peak value and wavelength of 0.995 and 1.24 μm are obtained, respectively, for $\mu_{c3} = 1.1$ eV.

In the last part, field distribution diagram is considered for Output3 port by considering $\lambda = 1.24$ μm , $w_3 = 15$ nm, $t_3 = 4$ nm, $g_3 = 0.2$ nm, and $\mu_{c3} = 1.1$ eV and would be shown in Fig. 16.

In this section, effects of structural parameters (w_1 , t_1 , g_1 , w_2 , t_2 , g_2 , w_3 , t_3 , and g_3) and chemical potentials (μ_{c1} , μ_{c2} , and μ_{c3}) on the transmission spectrum of different output ports (Output1, Output2, and Output3) were investigated (the transmission’s peak values and wavelengths were improved for the three output ports). In the following parts, the improved structures would be considered as biosensors for detection of different biological elements in blood samples.

Utilizing the Proposed Structure as Bio-sensors

In this part, the proposed structure would be considered as the biosensors for detection of different biological elements. The biological element would be introduced considering their refractive indices (RIs).

Output1 Port

In output1, different concentrations of glucose with various refractive indices are considered. The transmission spectrum is shown in Fig. 17.

The refractive indices (RI) utilized in Fig. 17 as 1.338, 1.352, 1.365, 1.375, 1.382, 1.394, and 1.405 are related to different glucose concentrations in blood samples ($n = 1.338$ for 25 mg/dl, $n = 1.352$ for 50 mg/dl, $n = 1.365$ for 75 mg/dl, $n = 1.375$ for 100 mg/dl, $n = 1.382$ for 125 mg/dl, $n = 1.394$ for 150 md/dl, and $n = 1.405$ for 175 mg/dl [40]).

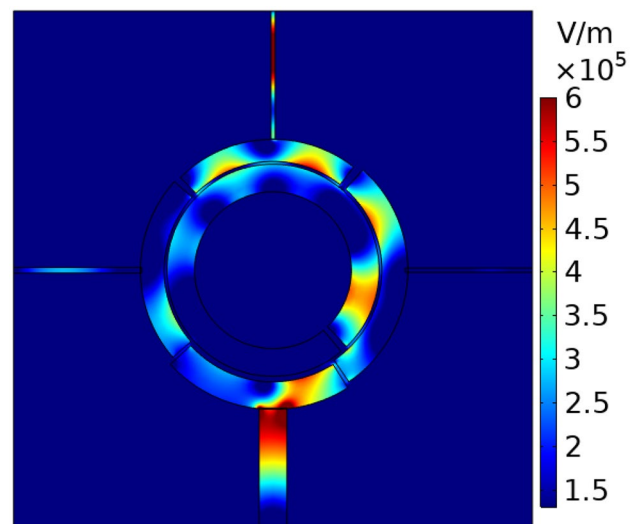


Fig. 16 Field distribution at $\lambda = 1.24$ μm for Output3 port

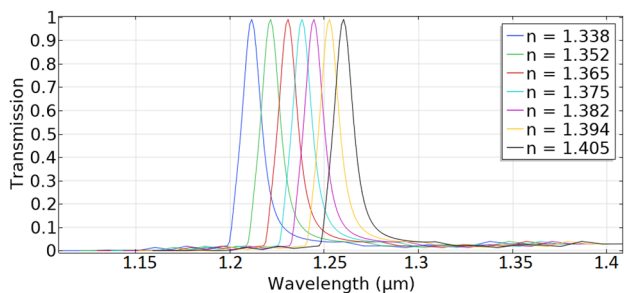


Fig. 17 Transmission spectrum versus wavelength for different glucose concentrations at Output1 port

As can be seen in Fig. 17, increasing RI would shift the transmission’s peak wavelength to higher values [2, 19]. The sensitivity factor can also be calculated considering the following equation:

$$S = \frac{\Delta\lambda}{\Delta n} (nm/RIU) \tag{9}$$

The sensitivity value of 1560 nm/RIU was achieved for output1 (for detection of glucose concentrations in blood samples). The figure of merit (FOM) can also be calculated as:

$$FOM = \frac{S}{FWHM} \tag{10}$$

FWHM=0.013 μm and FOM= 120 are achieved.

In the following part, output2 is considered for sensing cholesterol concentrations in blood samples.

Output2 Port

In this section, different concentrations of cholesterol with various refractive indices are considered and diagnosed in Output2 port. The transmission spectrum is depicted in Fig. 18.

The RIs utilized in Fig. 18 as 1.48, 1.485, 1.49, and 1.495 are related to different cholesterol concentrations in blood samples (*n* = 1.48 for 0.01%, *n* = 1.485 for 0.06%, *n* = 1.49 for 0.09%, and *n* = 1.495 for 0.13% [18]).

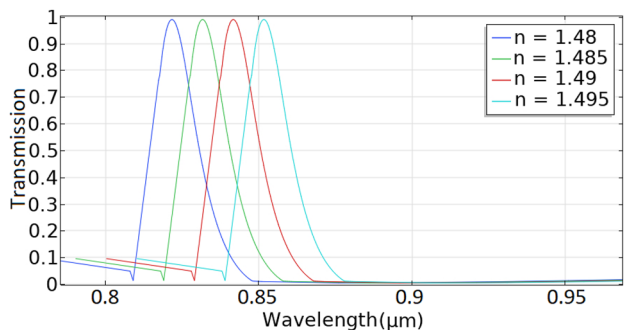


Fig. 18 Transmission spectrum versus wavelength for different cholesterol concentrations at Output2 port

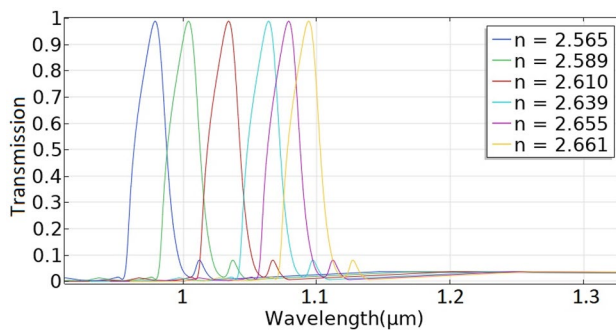


Fig. 19 Transmission spectrum versus wavelength for different creatinine concentrations at Output3 port

As can be seen in Fig. 18, by increasing RI, the transmission’s peak wavelength would be red-shifted.

Considering Eq. (7), the sensitivity value of 2666.6 nm/RIU was obtained for Output2 (for diagnosis of cholesterol concentrations in blood samples). FWHM=0.015 μm and FOM= 177.77 are achieved.

In the last part, Output3 is considered for sensing creatinine concentrations in blood samples.

Output3 Port

In this part, different concentrations of creatinine with various refractive indices are considered as biological elements. The transmission spectrum at Output3 port is depicted in Fig. 19.

The refractive indices (RI) considered in Fig. 19 as 2.565, 2.589, 2.610, 2.639, 2.655, and 2.661 are related to different creatinine concentrations in blood samples (*n* = 2.565 for 85.28 μmol/L, *n* = 2.589 for 84.07 μmol/L, *n* = 2.610 for 83.3 μmol/L, *n* = 2.639 for 82.3 μmol/L, *n* = 2.655 for 81.43 μmol/L, and *n* = 2.661 for 80.9 μmol/L [17]). The sensitivity value of 1458.3 nm/RIU was achieved for Output3 (for detection of creatinine concentrations in blood samples). FWHM=0.019 μm and FOM= 76.75 are achieved.

Table 2 indicates the comparison between the sensitivity factors of our proposed sensors for detection of glucose, creatinine, and cholesterol concentrations with some previously published works.

Table 2 Comparison of our proposed sensors with previous works

References	Sensitivity (nm/RIU)	FWHM (nm)	FOM
Glucose sensor [3]	1278	12.17	105
Glucose sensor [41]	225	10	20.45
Our proposed glucose sensor	1560	13	120
Creatinine sensor [27]	306.25	10	30.625
Creatinine sensor [42]	640.29	9.14	70
Our proposed creatinine sensor	1458.3	19	76.75
Cholesterol sensor [43]	156.18	15	10.41
Our proposed cholesterol sensor	2666.6	15	177.77

Conclusion

The novel structures based on the combinations of various U-shaped, split ring, and straight waveguides of SiO₂, Au, and graphene for detection of glucose, cholesterol, and creatinine were proposed and considered. The straight waveguides which were connected to the U-shaped waveguides were considered as the Input, Output1, Output2, and Output3 ports. The incident field (applied to Input port) was transmitted to the three output ports depending on the split parameters (α_1 , α_2 , α_3 , and α_4). Also, for improving the characteristics of the proposed bio-sensors (enhancing the transmission's peak value), effects of different structural parameters (w_1 , t_1 , g_1 , w_2 , t_2 , g_2 , w_3 , t_3 , and g_3) and chemical potentials (μ_{c1} , μ_{c2} , and μ_{c3}) were considered. Finally, the improved structures were utilized as bio-sensors for detection of glucose at Output1 port, cholesterol at Output2 port, and creatinine at Output3 port. Considerable sensitivity factors of 1560 nm/RIU, 2666.6 nm/RIU, and 1458.3 nm/RIU were achieved for glucose, cholesterol, and creatinine, respectively. FWHM and FOM of “13 nm, 120,” “19 nm, 76.75,” and “15 nm, 177.77” were obtained for glucose, creatinine, and cholesterol, respectively. As a result, the proposed structure can be considered as a suitable candidate for bio-sensing in optical integrated circuits.

Author Contribution All authors contributed to the study conception and design. Idea preparation, simulation, and analysis were performed by Esmat Rafiee and Roozbeh Negahdari. The first draft of the manuscript was written by Esmat Rafiee, and all authors commented on previous versions of the manuscript. All authors read and approved the final manuscript.

Data Availability This declaration is not applicable.

Declarations

Ethics Approval This declaration is not applicable.

Consent to Participate This declaration is not applicable.

Consent for Publication This declaration is not applicable.

Competing Interests The authors declare no competing interests.

References

- Das S, Singh VK (2022) Highly sensitive PCF based plasmonic biosensor for hemoglobin concentration detection. *Photonics Nanostructures - Fundam Appl* 101040. <https://doi.org/10.1016/j.photonics.2022.101040>
- Chahkoutahi A et al (2022) Sensitive hemoglobin concentration sensor based on graphene-plasmonic nano-structures. *Plasmonics* 17:423–431. <https://doi.org/10.1007/s11468-021-01531-5>
- Hajshahvaladi L, Kaatuzian H, Danaie M (2022) A high-sensitivity refractive index biosensor based on Si nanorings coupled to plasmonic nanohole arrays for glucose detection in water solution. *Opt Commun* 502:127421. <https://doi.org/10.1016/j.optcom.2021.127421>
- Kumar A, Kumar A, Srivastava SK (2022) A study on surface plasmon resonance biosensor for the detection of CEA biomarker using 2D materials graphene, Mxene and MoS₂. *Optik* 258:168885. <https://doi.org/10.1016/j.ijleo.2022.168885>
- Hajati Y (2020) Tunable broadband multi resonance graphene terahertz sensor. *Opt Mater* 101:109725. <https://doi.org/10.1016/j.optmat.2020.109725>
- Emami F et al (2019) Plasmonic multichannel filter based on split ring resonators: application to photothermal therapy. *Photonics Nanostructures - Fundam Appl* 33:21–28. <https://doi.org/10.1016/j.photonics.2018.11.006>
- Ho YZ et al (2012) Tunable plasmonic resonance arising from broken-symmetric silver nano beads with dielectric cores. *J Opt* 14:114010. <https://doi.org/10.1088/2040-8978/14/11/114010>
- Chau YF (2009) Surface plasmon effects excited by the dielectric hole in a silver-shell nanospherical pair. *Plasmonics* 4:253–259. <https://doi.org/10.1007/s11468-009-9100-8>
- Negahdari R, Rafiee E, Emami F (2018) Design and simulation of a novel nano-plasmonic split-ring resonator filter. *J Electromagn Waves Appl* 32(2018):1925–1938. <https://doi.org/10.1080/09205071.2018.1482240>
- Negahdari R, Rafiee E, Emami F (2019) Design and analysis of the novel plasmonic split ring resonator power splitter appropriate for photonic integrated circuits. *J Optoelectron Adv Mater* 21(2019):163–170
- Wang X et al (2014) Fabrication techniques of graphene nanostructures. *Nanofabrication Appl Renew Energy* 1–30. <https://doi.org/10.1039/9781782623380-00001>
- Bonaccorso F et al (2012) Production and processing of graphene and 2d crystals. *Mater Today* 15:564–589
- Kasani S et al (2019) A review of 2D and 3D plasmonic nanostructure array patterns: fabrication, light management and sensing applications. *Nanophotonics* 8:2065–2089. <https://doi.org/10.1515/nanoph-2019-0158>
- Zhang Z et al (2022) Plasmonic sensors based on graphene and graphene hybrid materials. *Nano Converg* 9. <https://doi.org/10.1186/s40580-022-00319-5>
- Lu H et al (2018) Flexibly tunable high-quality-factor induced transparency in plasmonic systems. *Sci Rep* 8:1558. <https://doi.org/10.1038/s41598-018-19869-y>
- Panda A et al (2020) Performance analysis of graphene-based surface plasmon resonance biosensor for blood glucose and gas detection. *Appl Phys A* 126. <https://doi.org/10.1007/s00339-020-3328-8>
- Aly AH, Mohamed D, Mohaseb MA, Abd El-Gawaad NS, Trabelsi Y (2020) Biophotonic sensor for the detection of creatinine concentration in blood serum based on 1D photonic crystal. *RSC Adv* 10:31765. <https://doi.org/10.1039/D0RA05448H>
- Jin YL, Chen JY, Xu L, Wang PN (2006) Refractive index measurement for biomaterial samples by total internal reflection. *Phys Med Biol* 51:371–379. <https://doi.org/10.1088/0031-9155/51/20/N02>
- Zhou S, Li X, Zhang J, Yuan H, Hong X, Chen Y (2022) Dual-fiber optic bioprobe system for triglyceride detection using surface plasmon resonance sensing and lipase-immobilized magnetic bead hydrolysis. *Biosens Bioelectron* 196:113723. <https://doi.org/10.1016/j.bios.2021.113723>
- Rakhshani MR, Mansouri-Birjandi MA (2017) High sensitivity plasmonic refractive index sensing and its application for human blood group identification. *Sens Actuators B Chem* 249:168–176
- Rakhshani MR, Mansouri-Birjandi MA (2017) Utilizing the metallic nano-rods in hexagonal configuration to enhance sensitivity of the plasmonic racetrack resonator in sensing application. *Plasmonics* 12:999–1006. <https://doi.org/10.1007/s11468-016-0351-x>
- Rakhshani MR, Mansouri-Birjandi MA (2018) A high-sensitivity sensor based on three-dimensional metal–insulator–metal racetrack

- resonator and application for hemoglobin detection. *Photonics Nanostructures - Fundam Appl* 32:28–34
23. Rakhshani MR, Mansouri-Birjandi MA (2018) Engineering hexagonal array of nanoholes for high sensitivity biosensor and application for human blood group detection. *IEEE Trans Nanotechnol* 17:475–481. <https://doi.org/10.1109/TNANO.2018.2811800>
 24. Moradiani F et al (2020) Systematic engineering of a nanostructure plasmonic sensing platform for ultrasensitive biomaterial detection. *Opt Commun* 474:126178
 25. Khani S, Hayati M (2021) An ultra-high sensitive plasmonic refractive index sensor using an elliptical resonator and MIM waveguide. *Superlattices Microstruct* 156:106970
 26. Khani S, Hayati M (2022) Optical sensing in single-mode filters base on surface plasmon H-shaped cavities. *Opt Commun* 505:127534
 27. Hossain M, Talukder MA (2021) Gate-controlled graphene surface plasmon resonance glucose sensor. *Opt Commun* 493:126994. <https://doi.org/10.1016/j.optcom.2021.126994>
 28. Pedrozo-Peñafiel MJ, López T, Gutiérrez-Beleño LM, Maia Da Costa MEH, Aucelio RQ (2020) Voltammetric determination of creatinine using a gold electrode modified with Nafion mixed with graphene quantum dots-copper. *J Electroanal Chem* 878:114561. <https://doi.org/10.1016/j.jelechem.2020.114561>
 29. Abdolmohammad-Zadeh H, Ahmadian F (2021) A fluorescent biosensor based on graphene quantum dots/zirconium-based metal-organic framework nanocomposite as a peroxidase mimic for cholesterol monitoring in human serum. *Microchem J* 164:106001. <https://doi.org/10.1016/j.microc.2021.106001>
 30. Shanbhag MM, Shetti NP, Malode SJ, Veerapur RS, Reddy KR (2021) Cholesterol intercalated 2D graphene oxide sheets fabricated sensor for voltammetric analysis of theophylline. *Flat Chem* 28:100255. <https://doi.org/10.1016/j.flatc.2021.100255>
 31. Sahraeian S et al (2021) Graphene-metal nanostructure as opto-fluid sensor. *Optik* 242:166713. <https://doi.org/10.1016/j.ijleo.2021.166713>
 32. Hanson GW (2008) Dyadic green's functions and guided surface waves for a surface conductivity model of graphene. *J Appl Phys* 103. <https://doi.org/10.1063/1.2891452>
 33. Yu Z, Veronis G, Fan S, Brongersma ML (2008) Gain-induced switching in metal-dielectric-metal plasmonic waveguides. *Appl Phys Lett* 92(4):041117
 34. Haus HA, Lai Y (1992) Theory of cascaded quarter wave shifted distributed feedback resonators. *IEEE J Quantum Electron* 28(1):205–213
 35. Zhong ZJ et al (2010) Sharp and asymmetric transmission response in metal-dielectric-metal plasmonic waveguides containing Kerr nonlinear media. *Opt Exp* 18:79–86. <https://doi.org/10.1364/OE.18.000079>
 36. Lu H, Liu X, Mao D, Wang L, Gong Y (2010) Tunable band-pass plasmonic waveguide filters with nanodisk resonators. *Opt Express* 18:17922–17927. <https://doi.org/10.1364/OE.18.017922>
 37. Chen J, Li Y, Chen Z (2014) Tunable resonances in the plasmonic split-ring resonator. *IEEE Photonics J* 4800706. <https://doi.org/10.1109/JPHOT.2014.2323294>
 38. Wang TB, Wen XW, Yin CP, Wang HZ (2009) The transmission characteristics of surface plasmon polaritons in ring resonator. *Opt Express* 17:24096–24101. <https://doi.org/10.1364/OE.17.024096>
 39. Xu Z et al (2018) Design of a tunable ultra-broadband terahertz absorber based on multiple layers of graphene ribbons. *Nanoscale Res Lett* 13. <https://doi.org/10.1186/s11671-018-2552-z>
 40. Panda A, Pukhrabam PD, Keiser G (2020) Performance analysis of graphene-based surface plasmon resonance biosensor for blood glucose and gas detection. *Appl Phys A* 16. <https://doi.org/10.1007/s00339-020-3328-8>
 41. Vafapour Z (2019) Polarization-independent perfect optical metamaterial absorber as a glucose sensor in food industry applications. *IEEE Trans Nanobioscience* 18:622–627. <https://doi.org/10.1109/TNB.2019.2929802>
 42. Gandhi S, Awasthi SK, Aly AH (2021) Biophotonic sensor design using a 1D defective annular photonic crystal for the detection of creatinine concentration in blood serum. *RSC Adv* 11:26655–26665. <https://doi.org/10.1039/D1RA04166E>
 43. Lu Y, Li H, Qian X, Zheng W, Sun Y, Shi B, Zhang Y (2020) Beta-cyclodextrin based reflective fiber-optic SPR sensor for highly-sensitive detection of cholesterol concentration. *Opt Fiber Technol* 56:102187. <https://doi.org/10.1016/j.yofte.2020.102187>

Publisher's Note Springer Nature remains neutral with regard to jurisdictional claims in published maps and institutional affiliations.

Springer Nature or its licensor (e.g. a society or other partner) holds exclusive rights to this article under a publishing agreement with the author(s) or other rightsholder(s); author self-archiving of the accepted manuscript version of this article is solely governed by the terms of such publishing agreement and applicable law.